

PIV and dynamic LES of the turbulent stream and mixing induced by a V-grooved blade axial agitator

Israel González-Neria^a, Alejandro Alonzo-García^{b*}, Sergio A. Martínez-Delgadillo^c, Víctor X. Mendoza-Escamilla^d, Juan Antonio Yáñez-Varela^a, Patrick G. Verdin^e, Gabriela Rivadeneyra-Romero^f

^a Posgrado en Ing. de Procesos, Universidad Autónoma Metropolitana Azcapotzalco, Av. San Pablo 180. Azcapotzalco, CP 07740 México D.F., Mexico

^b CONACyT-Centro de Ingeniería y Desarrollo Industrial, Carretera Champotón - Cd del Carmen 408, C. P. 24150 Ciudad del Carmen, Campeche, Mexico

^c Depto. Ciencias Básicas, Universidad Autónoma Metropolitana Azcapotzalco. Av. San Pablo 180. Azcapotzalco. CP 07740, México D.F., Mexico

^d Depto. Electrónica, Universidad Autónoma Metropolitana Azcapotzalco. Av. San Pablo 180. Azcapotzalco. CP 07740, México D.F., Mexico

^e Energy & Power, School of Water, Energy and Environment, Cranfield University, Bedfordshire, MK43 0AL., UK

^f Universidad del Istmo, Ciudad Universitaria S/N, Barrio Santa Cruz 4^a. Secc., Sto. Domingo Tehuantepec, Oaxaca, Mexico.

*Corresponding author:
Alejandro Alonzo-García
E-mail: alejandro_1980@hotmail.com

Abstract

The hydrodynamic behavior of a turbulent flow and the mixing characteristics generated by a V-grooved axial impeller inside an agitated tank reactor were investigated both experimentally and numerically. Angle resolved Particle Image Velocimetry (PIV) techniques with an angular displacement $\Delta\theta=5^\circ$ have been applied and two aerodynamic planes along the blades were considered. PIV-based results were compared to those obtained by Large Eddy Simulation (LES), used with the dynamic Smagorinsky-Lilly sub-grid scale (SGS) model. Results showed the existence of distinctive recirculation zones in the aerodynamic planes, and new additional frequencies in the impeller stream, induced by the grooves. A decrease of mixing time of about 11 % was obtained experimentally, consequence of the better suction induced by the grooved blades in the early stages of mixing. Mean velocities, vorticity, TKE obtained from LES showed a good agreement with the PIV-based results. The distributions of turbulence dissipation rate ε were similar to those obtained from PIV, however showing high under-predicted magnitudes.

Keywords: V-grooves; PIV; LES; turbulent flow; dissipation rate; axial impeller.

1. Introduction

Agitated tank reactors (ATRs) are extensively used in industrial processing, for applications such as powder dispersion, blending, flocculation, chemical reactions, polymerization, etc. The three-dimensional and time dependent characteristics of the turbulent flow field inside the vessel namely mean and fluctuating velocities, tip vortices, turbulent kinetic energy (TKE, also denoted k) and its dissipation rate ε are important parameters for the process efficiency. The homogeneity in a tank is difficult to achieve since the energy transferred from the impeller decays as the distance from the impeller increases, and zones with low velocities and turbulence are created in some parts of the vessel. The larger such zones within the ATR, the larger the time needed to perform mixing tasks. In a long time operation basis, this is also reflected by an increase of energy consumption of the device. The use of computational fluid dynamics (CFD) and turbulence modelling based on the Reynolds Averaged Navier-Stokes (RANS) approach has been commonly used to analyze the flow characteristics in ATRs. It is recognized that when using coarse grids, the mean velocities show a good agreement with experimental data, but the turbulent parameters are poorly predicted. The improvement of such predictions could therefore be achieved by increasing the number of cells in the numerical domain [1–4], although the prediction of the dissipation rate “ ε ” and its spatial distributions are among the main drawback of the k - ε family turbulence models in ATRs [5,6].

A more powerful approach which has been used in the past few years to enhance the accuracy of the turbulent parameters, is the Large Eddy Simulation (LES) [7]. This approach, based on the energy cascade of Kolmogorov, resolves directly the largest low frequency eddies, assuming that they contain most of the flow kinetic energy. According to Kolmogorov’s

theory, the smallest eddies, which dissipate energy by viscous effect, are universal and isotropic. In the LES model, such eddies are considered smaller than the cell sizes, and their influence is accounted by a Sub-grid Scale (SGS) model, under isotropic or anisotropic assumptions [8]. Thus, when a fine grid is used, the SGS model contribution on the response of the LES technique is expected to induce smaller errors than those of the RANS-based models. This technique has been successfully applied in ATRs to model the flow induced by different radial or axial impeller models [9–12] in systems composed of one or two turbines [13,14]. Good agreement between experimental measurements with Particle Image Velocimetry (PIV) or Laser Doppler Anemometry has been obtained for flow parameters such as velocities, circulation patterns, mixing time, vortex trajectories, TKE, shaft power and turbulence intensities. The complexity of the flow near the impeller blades has captured the attention of several researchers [15,16]. In the vicinity of the region where the momentum of the blades is transferred to the fluid, a particular phenomenon takes place; the formation and evolution of trailing vortices.

From a CFD perspective, Delafosse et al., compared the response of LES and Standard $k-\epsilon$ models in the flow induced by a Rushton turbine. They pointed out the superiority of the LES model to reproduce the vortex formation and trajectories when results are compared to PIV measurements [15]. Considering that vortical structures are responsible for much of the turbulence production in ATRs, their behavior must be assessed adequately. Over the years, numerous studies have been performed to understand flow patterns and turbulence characteristics of radial and axial impellers under different geometrical configurations see, for instance, Yoshi et al. [5,17]. However, for the case of trailing vortices, most of the published research gravitates around radial pumping devices [15,18–20]. In addition,

modelling approaches applied to straight blade impellers are usually not optimized to deal with curved or folded blades [4]. Steiros et al. proposed the use of fractal impellers to reduce the power consumption in radial turbines. They concluded that the interaction of the blade wake had no relevance in the reduction of the torque [21]. In addition, the fractal geometry walls can break the symmetry in the locations of the two main tip vortices, the upper one being the weaker. The weaker vortex causes a pressure recovery in the recirculation zone located behind the impeller, which in turn, leads to drag reduction. Recently, Başbuğ et al. performed Direct Numerical Simulation (DNS) to acquire detailed information on the trailing vortices and their effect on the pressure field around a rectangular and fractal bladed radial flow impeller [22]. They found out that the fractal blades create jets which form several weaker vortices that on average, cause a smaller and weaker recirculation zone behind the blades, reducing drag.

The aerodynamic control of flow behavior has been thoroughly investigated for a long time for aircraft applications, because of its relations with energy saving. One way to deal with this aerodynamic control is to modify the surface of the body and use it as a passive control method. Lim and Lee investigated the variation of the drag force and the wake structure behind a cylinder covered with U and V grooves [23]. They showed that grooves lead to a drag reduction because of modifications in the wake velocities due to the delay of separation; this phenomenon is also associated with an elongation of the vortex formation regions.

Considering the similitude as blunt body of a circular cylinder with a pitched bladed turbine, and in order to explore benefits that grooves cause in the wakes of blunt bodies on mixing, the mixing time, and the turbulent flow induced by a V-grooved pitched blade turbine are investigated via 2D Particle Image Velocimetry (PIV) and LES.

A complete analysis of the turbulent flow structures induced by both the standard four bladed pitched blade turbine (4PBT) and a V-grooved impellers is performed. Measurements using angle resolved PIV at 5° intervals and those derived from two new aerodynamic planes (the first one between the blade, and the second one near the tip) are presented. These aerodynamic planes are the result of a superimposition of contours from two PIV measurements, creating one unique contour, similarly to the PIV multi-block approach, which combines one large contour from several sub-maps. In a previous work from our group, it was stated that grooved impellers deliver drag reduction in a wide range of Re , and measurements of velocities and turbulence have been presented for two grooved models [24]. As an extension of such previous work, and in order to understand deeper the turbulence nature and mixing induced by grooves, new measurements of TKE and ε in several planes are presented, taking the V-grooved model as representative. Also, the numerical response of the LES model with the dynamic Smagorinsky-Lilly SGS is assessed. This is especially of interest as most studies reported in the literature have been performed for straight blade impellers. A turbulence model which works well for a specific impeller design, is not necessary optimum for another design based on folded blades. Finally, the mixing time, which is another important and useful parameter to describe the impeller performance, has been evaluated experimentally through changes in conductivity, and numerically via LES.

2. Experimental and numerical methodology

2.1 Impeller design and agitated tank characteristics

Two different blades were used in this study. The first one, the base line (4PBT), is a standard 4 bladed pitched blade turbine (45°) of diameter $D=0.08$ m and 1.5 mm thick, as shown in Fig. 1a. The second blade, which shows a new design, has grooved surfaces with triangular

shapes and sharp peaks. The dimensions of this new blade were established as a function of the blade width ($w=14.3$ mm), see Fig. 1b.

The experimental system consists of a cylindrical acrylic tank of diameter $T=0.25$ m, comprising four $0.1T$ wide, 3.0 mm thick baffles, equally distributed around the tank periphery. In agreement with the literature, the cylindrical tank was placed inside a square one, to reduce refraction. The working fluid was water at laboratory conditions ($\rho=998.2\text{kg/m}^3$ and $\mu= 1.003\text{mPa}\cdot\text{s}$) and the free surface height was fixed at $H=T$. The impellers were located at a clearance $C= T/3$, the rotational speed was set at 500 rpm or $N=8.333$ rev/s, achieving fully turbulent flow conditions ($Re = \rho ND^2/\mu = 5.2 \times 10^4$) [25].

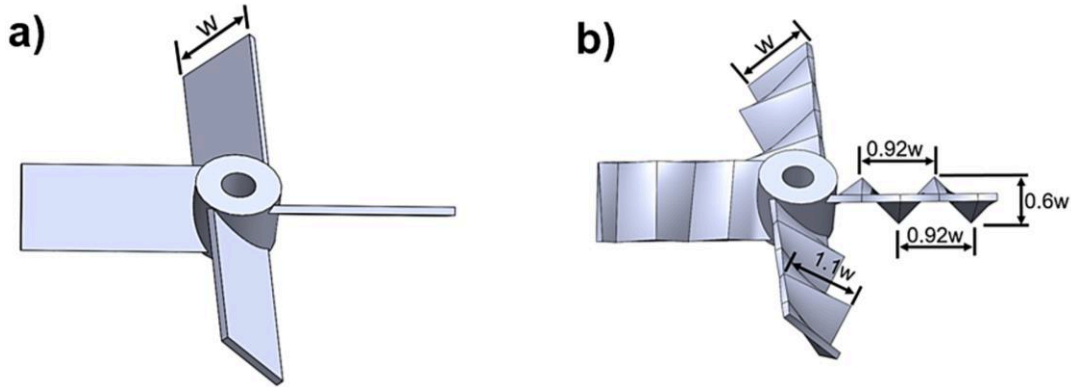


Fig. 1 Impeller geometrical description: a) 4 PBT model, b) V grooved model.

2.2 PIV measurements

2.2.1 PIV set-up

Experimental velocity and turbulence maps in the radial-axial stream plane were obtained using angle resolved measurements. To obtain the angle resolved measurements, data were recorded on 18 planes located between two blades, with an angular displacement $\Delta\theta=5^\circ$, starting at $\theta=0^\circ$, as shown in Fig. 2a. To extent the analysis further, two additional planes

were considered in the tangential-axial direction to explore the mid-plane (MP) and tip-plane (TP) aerodynamics, see Fig. 2b.

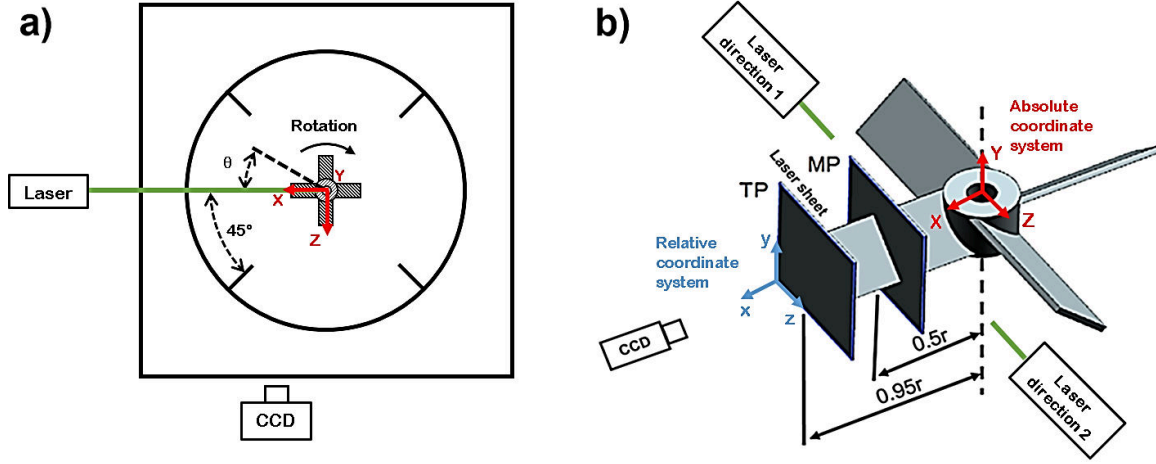


Fig. 2 PIV measured plane: a) angle resolved PIV setup, b) The mid-plane (MP) and tip-plane (TP) aerodynamic planes located along the blade span.

The data recording of these planes was obtained twice, with only a difference in the position of the laser (laser direction 1 and laser direction 2), as shown in Figs. 3a and b. In all results obtained on the MP and TP, final data from the first measurements (laser direction opposite to the blade rotation) were finalised by mapping the missing information in the shadow region with the second set of measurements (data inside the dashed rectangle region in Fig. 3b), to form a single semi-continuous contour. This procedure was applied to capture missing data from the first measurements due to the blade interference on the laser sheet, forming this “shadow region”.

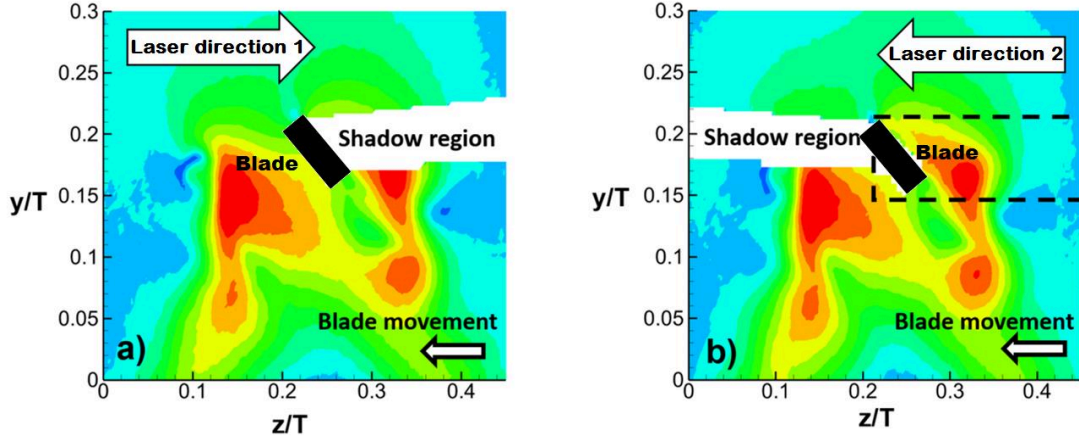


Fig. 3 Description of the composition of the MP and TP velocities and turbulent maps: a) The laser device triggers opposite to the blade rotation, b) The laser is in the same direction as the blade rotation.

The PIV system (TSI Incorporated) is composed of a CCD camera (2360 px x 1776 px) with 50 mm lenses, a synchronizer and a double-pulse Nd:YAG laser (wavelength of 532 nm and energy pulse of 75 mJ). Hollow glass spheres with silver coat of approximate 10 μm diameter and density $\rho=1020 \text{ kg/m}^3$ were used as seeding particles. Pictures were taken every $\Delta t=100 \mu\text{s}$ and the capture rate was fixed to 14 frames/s. The TSI Insight 4G software was applied to analyze the images via the Nyquist recursive grid algorithm, with an interrogation window of 32×32 pixels and a 50 % overlap between them. The size of all the measured planes was around $101 \text{ mm} \times 75 \text{ mm}$, with vector resolutions of $43 \mu\text{m/px}$ for the angle resolved planes, and $51 \mu\text{m/px}$ for the tangential-axial ones. Flow parameters were obtained from the average of 400 pairs of images taken at each plane.

2.2.2 Power number and pumping number from torque-meter and PIV

The power number N_p was calculated from eq. (1) by using the shaft power derived from $P=2\pi NT$. After achieving steady conditions, 900 torque T values were collected at a frequency of 50 Hz using a Futek-FSH1980 torque-meter, which has a maximum capacity of 1.41 N·m, use temperature control, and has a precision of 0.5 %.

$$N_p = \frac{P}{\rho N^3 D^5} \quad (1)$$

Where N is the shaft speed in rev/second and D is the impeller diameter in meters.

The pumping number was calculated from eq. (2).

$$N_Q = \frac{Q}{\rho N D^3} \quad (2)$$

The experimental mass flow Q of each impeller was obtained from the phase averaged axial velocity maps, by integrating the axial velocity V_a profile in the radial direction along a line located 2 mm below the impeller blades:

$$Q = 2\pi\rho \int_0^R V_a r dr \quad (3)$$

Also, the pumping effectiveness η_E was used in order to assess the pumping of the impellers per unit power consumption [26]:

$$\eta_E = \frac{N_Q}{N_p} \quad (4)$$

2.2.3 Assessment of κ and ε from PIV measurement

For the analysis of turbulent parameters, the triple decomposition procedure was implemented to the PIV data to obtain velocity fluctuations without the wave effects induced by the blades rotation. Thus, the periodic component was removed from the fluctuating velocities using eq. (5).

$$u'' = U - \langle \tilde{u} | \theta \rangle \quad (5)$$

where U is the instantaneous velocity at a fixed angular position, $\langle \tilde{u} | \theta \rangle$ is the phase averaged velocity, and u'' is the velocity fluctuation, free from the periodic wave influence [27,28].

Similarly, the fluctuating velocities for the turbulent kinetic energy TKE (or k) and the dissipation rate ε were calculated by considering $u' = u''$, i.e. considering the processed

fluctuations free from the influence of the periodic motion. In the present study, the simplified method proposed by Khan et al. was adopted in order to assess the TKE [29]. This approach uses the two components of the fluctuating velocity measured by PIV, and estimates the influence of the third term, considering pseudo-isotropic assumptions, according to eq. (6).

$$k = \frac{3}{4}(\overline{u'^2} + \overline{v'^2}) \quad (6)$$

Since the interrogation window size of the PIV is about 28 times the Kolmogorov length scale $\lambda_K = (v^3/\bar{\varepsilon}_T)^{1/4}$, sub-predictions of ε are expected if the direct evaluation method is applied, thus, the large eddy approach proposed by Sheng et al. was implemented [30]. In this method, the contribution of scales smaller than the length of the interrogation window “ Δ ” of the PIV are modeled by a SGS model which compensates ε values. Based on the same pseudo-isotropic assumption for TKE, eq. (7), as defined by Khan, was applied [31].

$$\varepsilon = (C_s\Delta)^2 \left(4 \left(\frac{\partial u'}{\partial x} \right)^2 + 4 \left(\frac{\partial v'}{\partial y} \right)^2 + 2 \left(\frac{\partial u'}{\partial y} \right)^2 + 2 \left(\frac{\partial v'}{\partial x} \right)^2 \right)^{3/2} \quad (7)$$

According to Meyers and Sagaut, it is required to adjust the Smagorinsky constant C_s depending on the ratio Δ/λ_k [32]. For the angle resolved measurements, the ratio Δ/λ_k was estimated to be ≈ 30 , whereas for the mid and tip plane measurements the value was ≈ 35 , corresponding to $C_s \approx 0.16$, and $C_s \approx 0.164$ respectively. Thus a fixed value of $C_s = 0.16$ was applied in eq. (7). The ε maps are normalized with the averaged specific dissipation $\varepsilon^* = \varepsilon/\bar{\varepsilon}_T$, and $\bar{\varepsilon}_T$ was estimated from the torque meter measurements at each impeller using the relation $\bar{\varepsilon}_T = P/m$, with m being the mass of water.

2.3 Numerical simulation

2.3.1 Numerical details

The LES model is based on the assumption that the large eddies, which contain most of the flow energy, are dependent on the geometry and transport most of the flow momentum and mass, while the smallest dissipative eddies are considered isotropic and universal. Under this basis, LES resolves directly the larger eddies contained in the flow, implicit on the set of Navier-Stokes equations with filtered variables, being that the smallest eddies, whose scales are smaller than the filter width or grid spacing, are accounted for in the equations by a SGS stress tensor " τ_{ij} ". In this work, the dynamic Smagorinsky-Lilly model was used to resolve the smaller eddies [33]. This model computes the Smagorinsky constant C_s dynamically using information of the resolved eddies. By doing so, the problem of a non-zero turbulent viscosity related to the utilization of a constant value (i.e. $C_s=0.1$) at the walls is avoided. An alternative strategy is to use a function which damps the turbulent viscosity at the walls, for example the Van Driest damping function. However, this approach does not necessary lead to better predictions of flow quantities as the asymptotic behavior of the SGS viscosity in the near wall regions is not well reproduced [9].

The numerical simulations were conducted with the commercial software FLUENT V.15.0. The sliding mesh technique was applied to replicate the impeller movement. A full three dimensional model of the ATR including the impeller and all 4 baffles were built using tetrahedral cells with the ANSYS Meshing tool. Two meshes were built, the first one composed of 3.26 M cells for the 4PBT test cases and the second one composed of 3.62 M cells for the V-model. In order to capture the trailing vortices near the impellers which are responsible for high turbulence levels in the discharge and the enhancement of mass and

momentum transport, the rotational cell zone domains were refined; 1.88 M (58 %) cells and 1.92 M cells (52 %) were clustered in such regions for the 4PBT and V-model respectively. The nodal cell distribution in the impeller blades was imposed to be uniform with a nodal spacing in the range 0.25-0.35 mm, which is below the 0.4-0.5 mm range used by Yeoh et al. [9]. For the current mesh, five nodes were disposed along the blade thickness, and a growth ratio of 1.20 was imposed in the impeller blades. The highest skewness obtained for the grids were of 0.76 and 0.8 for the 4PBT and V-model respectively, both below the 0.95 value recommended by the grid generation guidelines from ANSYS [34].

The average normal nodal distance in wall units of the nearest impeller cells was estimated around $y^+ \approx 2.5$ for both impeller model domains. The final generated mesh of the V-model is shown in Fig. 4. It is noteworthy to mention that the recommended value of $y^+ < 1$ using additional adaption refinements was not affordable as grid sizes, and therefore computational times, increased substantially by a factor of 2 or 3. Although a grid independence analysis is desirable in CFD modelling, this is not common practice when the LES method is applied as it involves high computational costs, especially when statistical convergence solutions are needed, see for instance the work of Jahoda et al. [35], Min and Gao [36] and Zadghaffari et al. [37] where one grid only has been used.

In this work, the nodal spacing was based on the grid independence study performed previously for the analysis of RANS based models (MF grid of 2.36 M cells in [38]), but with additional refinements.

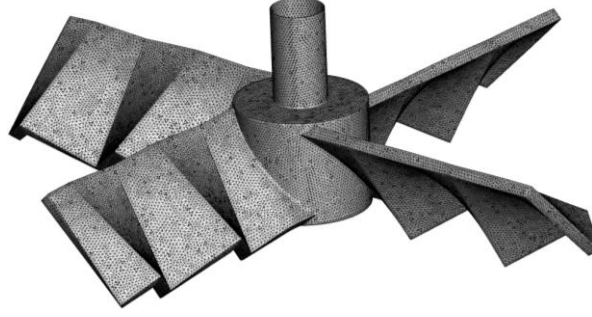


Fig. 4 Isometric view of the cell arrangement disposed on the V-model impeller.

The pressure-velocity coupling was selected with the SIMPLE algorithm and the bounded central differencing method was applied to the spatial discretization of the momentum equation. A non-slip boundary condition (BC) was imposed with standard log-law wall functions on all walls of the domain (impeller, shaft, tank walls and baffles), and the fluid free surface was treated as a zero stress wall (symmetry boundary condition).

The temporal term was discretized by the second order implicit algorithm. Prior to running the dynamic LES model and in order to accelerate statistical convergence, the flow solution was initialized with the solution from the Realizable $k-\varepsilon$ based model run with the Multiple Reference Frame approach (MRF). Finally, results were obtained from statistics collected from 30 impeller rotations, taking 1° of blade angular displacement ($\Delta t = 3.333 \times 10^{-4}$ s). Each time step was obtained using 30 sub-iterations and a 10^{-5} convergence criterion was set for all equations. Note that the blade angular rotation applied between time steps (1°) is below the 4° used in the work of Bakker and Oshinowo [13] and the 5° used by Li et al. [39]. In addition, such temporal resolution is smaller than the Kolmogorov time scale $\tau_K = \sqrt{\nu/\bar{\varepsilon}_T}$ estimated as 2.16×10^{-3} s for the 4PBT impeller, and 2.24×10^{-3} s for the V-model.

2.3.2 LES calculation of the turbulence parameters, power and pumping number

The resolved non-filtered scale of TKE was obtained by:

$$k_{RES} = \frac{1}{2} (\overline{u'^2} + \overline{v'^2} + \overline{w'^2}) \quad (8)$$

where u' , v' and w' are the fluctuating velocity components in the x , y and z directions.

The SGS modeled TKE was calculated with:

$$k_{MOD} = \overline{\left(\frac{\mu_{turb}}{\rho C_{dyn} \Delta} \right)^2} \quad (9)$$

where μ_{turb} is the turbulence viscosity, C_{dyn} is the SGS dynamic constant and Δ is the cubic root of the cell volume.

To compare with the PIV profiles and maps, the total time averaged TKE defined by eq. (10) was used to assess the LES predictions.

$$k_{total} = k_{RES} + k_{MOD} \quad (10)$$

At each time step, the total dissipated power in the vessel was derived from the numerical volume integral given by eq. (11)

$$P_{LES} = \int (\mu + \mu_{turb}) S^2 dV \quad (11)$$

The contours of dissipation rate ε_{LES} were obtained by creating a custom field function accounting for the product of the sum of the molecular and SGS kinematic viscosities by the squared strain rate S :

$$\varepsilon_{LES} = (\nu + \nu_{turb}) S^2 \quad (12)$$

The time-average values obtained from eq. (12) are used for the PIV comparisons using their non-dimensional form $\varepsilon^* = \varepsilon_{LES} / \bar{\varepsilon}_T$. The LES based calculations of N_P were obtained from the time average values of torque monitors imposed at each impeller, and from the predicted time average dissipated power P_{LES} . Finally, the Q used for N_Q (implicit in η_E) was obtained

from the time average mass flux through a circular surface of diameter D projected 2 mm below the impeller blades.

2.4 Mixing time measurements and simulation

To assess the transient behavior of the mean flow produced by the impellers, mixing time was evaluated. The results of the velocity field obtained with the dynamic LES simulation were used as starting point to resolve the scalar field of the concentrations. To simulate the tracer injection a sphere patch with a radius of 2 cm was defined in the mesh at 22 cm from the bottom wall and 6 cm in the radial coordinate from the axis. The tracer was defined with the same properties of the water and with a typical value for liquids of the molecular diffusivity coefficient (10^{-9} m²/s). The numerical schemes used to resolve the transport of species was the same than the use in the dynamic LES simulation. Criteria convergence for monitors were fixed at 10^{-4} for all variables. For both models, six seconds were simulated using a $\Delta t=0.01$ s and 50 sub-iterations. The monitoring points were arranged at the same positions that the probes in experimental tests. In experiments, mixing time was estimated using the tracer technique with saturated solution of NaCl. Two conductivity probes were fixed 22 cm high from the bottom of the tank and 6 cm far from the center. These probes were positioned at a 45° angle from the point of injection. Both transient profiles, conductivity from the experiments and mass fractions from the simulations, were used to calculate the mixing time when the uniformity reached 95%.

3. Results and discussion

3.1 Angle resolved velocity components and vorticity – (PIV vs CFD)

Fig. 5 shows the PIV results and the corresponding LES profiles of non-dimensional axial velocity and vorticity at the representative angle resolved planes 0° , 40° and 60° . The dimensionless vorticity ω^* was obtained by dividing the z-vorticity by the blade passage frequency ($\omega_{rot} = 33.3$ Hz). At 0° , there is no important difference in the parabolic V_a profile measured by PIV, independently of the impeller design. However, the V-model enhanced ω^* in most locations, reaching the maximum value $\omega^* = 3.8$ at $x/D = 0.8$. This value is considerable larger than the $\omega^* = 0.4$ value obtained with the 4PBT model. A plausible explanation of this effect is provided by the streamlines shown in Fig. 6, where several highly rotational regions present near the peaks and valleys of the V-model are not obtained for the straight blade impeller case. Negative values of ω^* present in the $0 < x/D < 0.4$ regions are attributed to the secondary recirculation bubble formed inside the core region of the stream which has been reported in axial impellers [1,4]. In the 40° plane, axial velocity profiles of the V-model suffered attenuations in the interval $0.37 < x/D < 0.77$ and a convex velocity region is formed. For both impellers, the maximum peaks of velocity increase from $V_a/V_{tip} = 0.45$ at 0° plane to $V_a/V_{tip} = 0.55$ at 40° , indicating a dependence of the maximum magnitude with the angle. Also, the parabolic profile collapsed along the radial positions. The increase of maximum values is more visible in the vorticity profiles, where values reached about 9.0 and 7.5 for the 4PBT and V-model respectively, in comparison to the 0.5 and 3.8 present at 0° . Near the hub and along the first third of the blade, vorticity profiles showed irregular shapes and several negative peaks of ω^* are visible, indicating the creation of new vortices. The velocities of the concave region of the V-model on the 40° plane recovered at 60° , and

velocity profiles were similar for both impellers. An attenuation in the magnitudes was present for both V_a and ω^* .

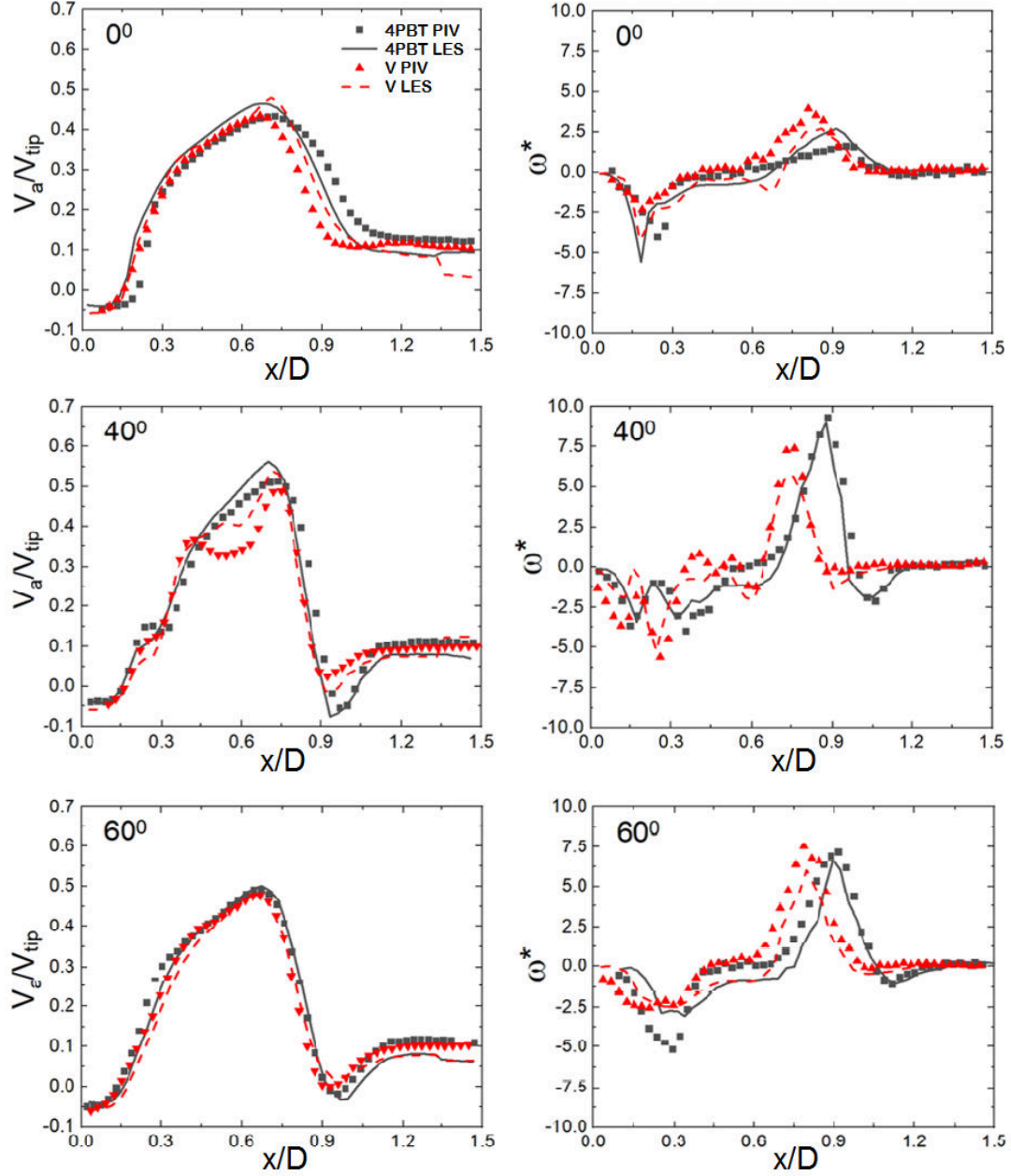


Fig. 5 Axial velocity and vorticity profiles obtained from a line 3 mm below the impellers at 0°, 40° and 60° angle resolved planes.

LES results of V_a were in good agreement with PIV measurements. In the near tip region ($0.6 < x/D < 1.2$) where the trailing vortices are detached, the numerical model adequately predicted the PIV ω^* profiles. Thus, the LES model was able to replicate mean velocities and spatial derivatives reflected in the vorticity profiles, along with their angular evolution, not only for the regular straight blade impeller, but also for the grooved surfaces blade impeller.

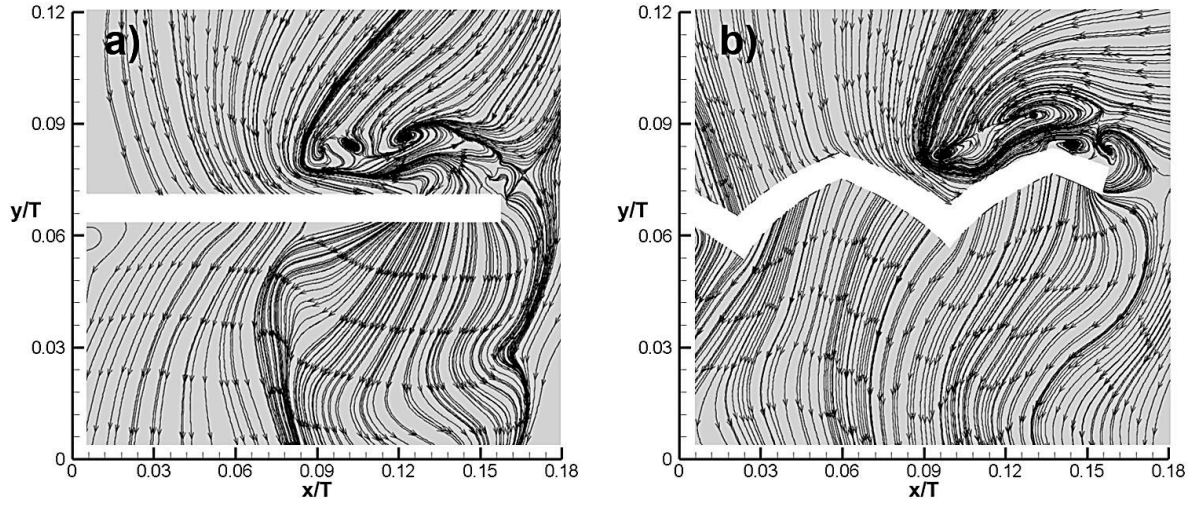


Fig. 6 Streamlines obtained at 0° plane: a) 4PBT model, b) V-model.

3.2 Angle resolved turbulence production and dissipation rate

The non-dimensional profiles of TKE in Fig. 7 shows the trends observed of V_a and ω^* for both impellers. For each angular position, values of TKE are similar for both impellers. In the 40° plane, the most significant gradients are present in the near hub locations. Depending on the impeller model, the radial locations of maximum TKE are however shifted. This is clearly visible on the 0° and 40° planes, where the maximum TKE is seen at $x/D=0.75$ for the V-model, whereas the location of the peak for the 4PBT model is obtained at $x/D=0.9$. Again, the LES predictions are fairly close to the experimental values in most of the positions.

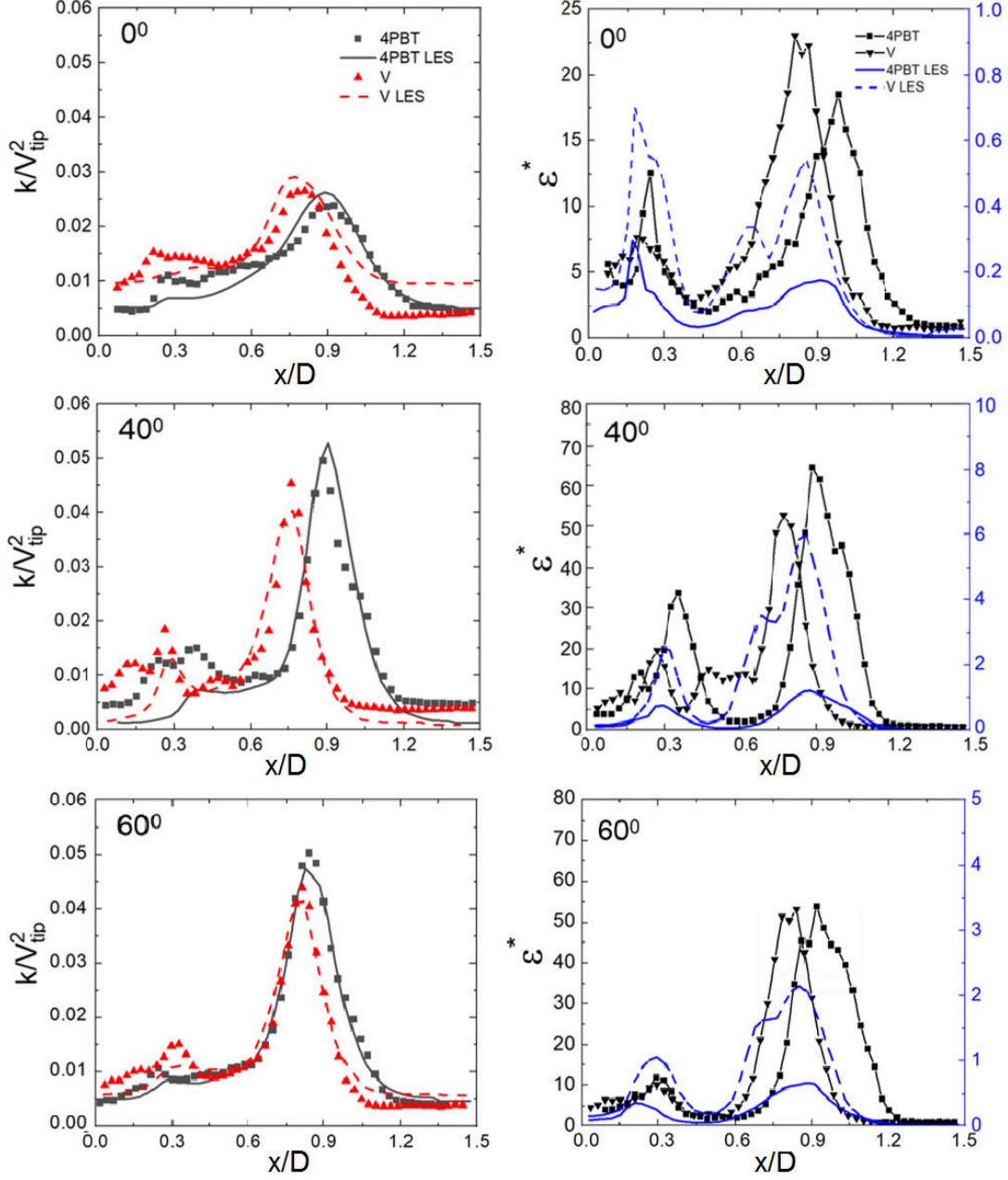


Fig. 7 Non dimensional TKE and dissipation rate profiles from a line 3 mm below the impellers at three angle resolved planes.

The validity of the pseudoisotropic assumption was checked by plotting the profiles of $\overline{(w')^2} = [\overline{(u')^2} + \overline{(v')^2}]/2$ from PIV vs the numerical value, on a line located 10 mm below the V-model impeller at $\theta=0^\circ$, as shown in Fig. 8. A good agreement is observed for

$0.45 < x/D < 1$, but differences larger than 100 % were present near the hub at $0 < x/D < 0.2$. These discrepancies highlight the fact that any deeper analysis will require the assessment of other angular positions, the mid and tip z-y planes and the two impeller models; this is however outside the scope of this work.

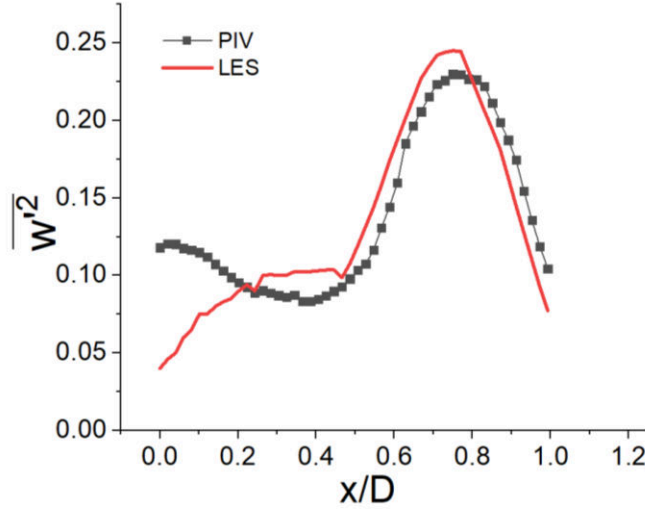


Fig. 8 Normal plane fluctuating velocity component profiles obtained at a line 10 mm below the V model impeller.

The ε^* profiles of the V-model impeller show larger magnitudes on the 0° plane in most x/D locations compared to the 4PBT model. On the 40° plane, the ε^* values increase for both impellers, reaching $\varepsilon^*=67$ for the 4PBT model and $\varepsilon^*=53$ for the grooved one. In contrast to the 0° plane, the 4PBT model presents larger ε^* magnitudes for most locations, except for the region between $0.45 < x/D < 0.8$. The peak value of the 4PBT impeller is slightly attenuated on the 60° plane and the only difference between impeller profiles is the location of the peaks, which are closer to the hub, similarly to the TKE profiles on the 0° and 40° planes. The LES predictions of ε^* follow qualitatively the trends captured by the PIV measurements. Magnitudes which increased in the 40° plane, are slightly attenuated in the 60° plane, and the

shape of the profiles are similar. Also the LES predictions with the V-model show larger values than those obtained with the 4PBT model. This suggests that there is an increase of ε near the V-model impeller stream, which is related to the formation of new recirculation zones in the vicinity of the impeller walls, as discussed in the previous section. From a quantitative point of view, all LES values were drastically sub-predicted. As shown in Table 1, when comparing the N_p from ε with the corresponding value derived from torque-meter, 23 % and 24 % only of the real dissipated power were captured by the LES model for the 4PBT and the V-model, respectively. A possible cause for such low levels is the number of cells of the grids, as a dependence of cell number and ε levels has been recognized for most turbulence models [3,4]. For example, G. Lane [4] modeled 1/3 of a tank using the DES model in a domain composed of 13.1 M cells, and reported that with such grid refinement, 69 % only of the real dissipation was predicted [40]. The DES model works similarly to LES except in the vicinity of solid walls, where the boundary layer is solved with a RANS based model. Under-predicted values were therefore expected in the CFD results, as reported here. The comparison of the maximum values of ε^* as function of the angle is shown in Fig. 9. From the PIV, the V-model caused larger values in comparison to the regular 4PBT in the range of 30°-50°, where values were around 55-65 in comparison to those of 38-55 for the 4PBT. Between 0° and 20° a slight increase of ε^* was present for the V-model. On the other hand, the results were opposite in the range 60°-75°. The difference between the angular locations of maximum ε^* is related to differences in vortex dynamics caused by modifications of the boundary layers induced by the grooves. Although showing lower levels than those experimentally present, the intensification of ε^* caused by the grooved walls was also present in the LES predictions. In this case, the ε^* values obtained with the V-model were larger at all positions, except on the 55° plane. Thus, the LES model followed the experimental trends,

though qualitatively. One possible reason of the differences in magnitude between PIV measurements and LES, could be due to the LES-PIV approach, which captures more dissipation in comparison to the Direct Evaluation Method [27], which has been used in other studies to validate numerical predictions, see for instance Yeoh et al. [9], and Baldi et al., [41]. Looking further into the work of Baldi et al., the spatial resolution of their correlation windows was 5.8 times the λ_K , and therefore, under-predicted values were expected from their measurements [42]. Finally, the deviations in the angular evolution of maximum ε , are believed to be a consequence of a different spatial distribution of vortical regions predicted numerically in comparison to that of PIV. This could again be a consequence of the grid refinement, especially in the rotational region, the SGS behavior, or a problem inherent to the y^+ . Additional work would however be required to explain this in detail.

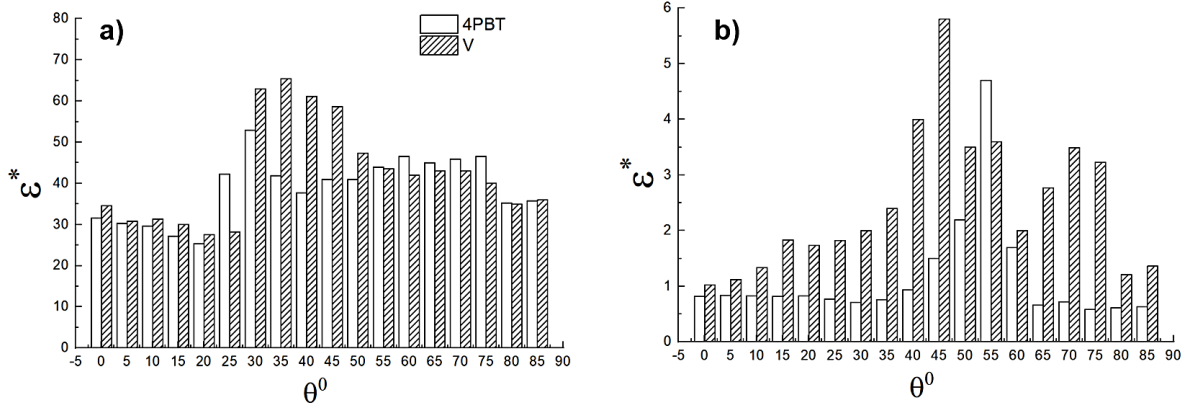


Fig. 9 Maximum dissipation rate magnitudes for different angles: a) PIV measurements, b) Predicted by LES.

3.3 Aerodynamic analysis in the mid-blade and tip-blade planes

Figs. 10 and 11 show the non-dimensional V_a and ω^* maps obtained by PIV and LES simulations at the mid and tip planes of the blade. In this section, ω^* refers to the x-vorticity component divided by the blade passage frequency. A good match between the PIV blocks used to create the contour maps is obtained for all parameters. Fig. 10a shows the non-dimensional axial velocity contours obtained at the mid-blade plane. Here, the 4PBT model shows larger V_a gradients compared to the V-model in the front and rear regions of the impeller. Two elongated high V_a spots are formed in the axial direction for the V-model. Both impellers show two peculiar lateral spots of low velocity aside the high V_a regions. In the tip-blade plane, the effect is the opposite, and the V-model impeller presents a larger region of high V_a below the impeller. In both cases, the low velocity lateral spots are located near the blade.

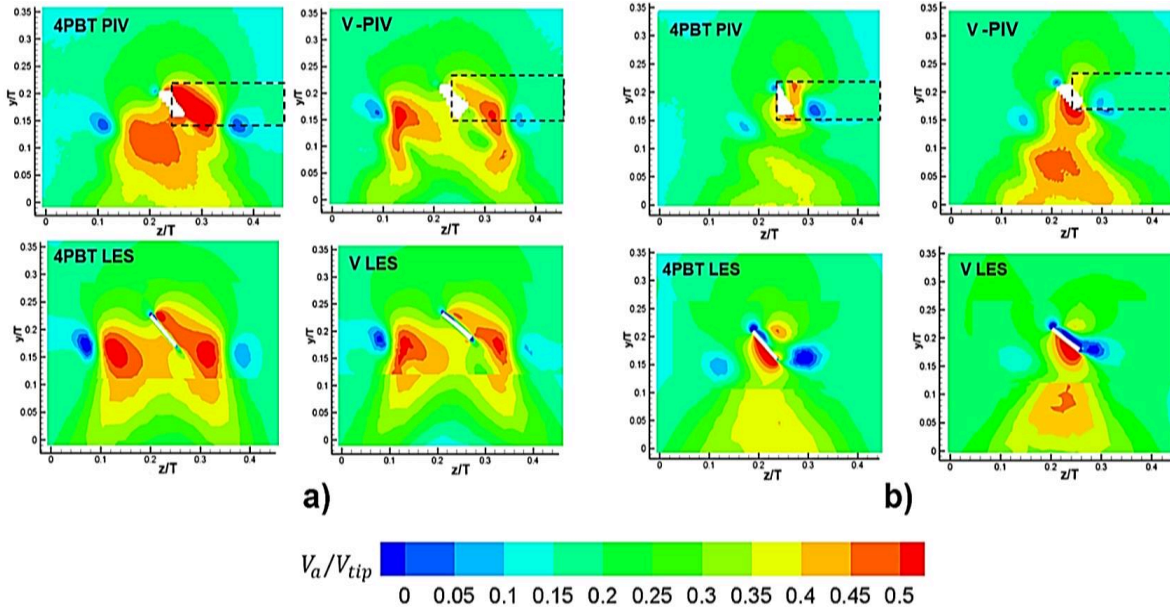


Fig. 10 Axial velocity maps obtained from PIV and CFD: a) Mid-blade plane, b) Tip-blade plane.

Fig. 11a shows additional high ω^* regions visible in the front and rear regions of the mid-plane for the V model when compared to the 4PBT. In the tip-plane, ω^* values are smaller than those of the mid-plane, and the number of vortices decreases for both impellers. Here, slightly larger ω^* values are present for the V-model than for the 4PBT model (see vortices 2 and 3 in Fig. 11b). Also, the recirculation extent of the 4PBT model is larger than that of the V-grooved model, causing a larger pressure drop behind the blade tip which is reflected by an increase of drag. Although slightly distorted, the LES model was also able to reproduce most of the vortical regions measured by PIV in the front regions (see vortices 1-4 in Fig. 11a, and 1-3 in Fig. 11b). However, in the rear regions of both impeller models, some vortices were not fully detached or were much smaller than those measured.

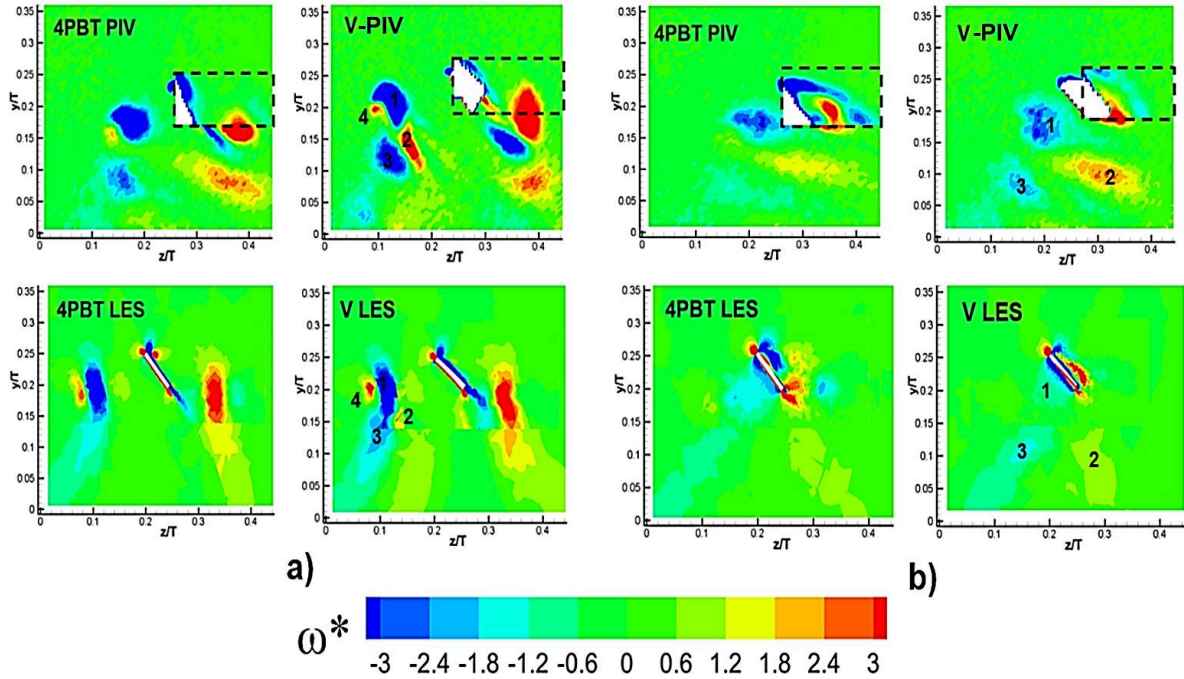


Fig. 11 Non-dimensional x-vorticity component maps from PIV and LES: a) Mid-blade plane, b) Tip-blade plane.

The non-dimensional mid-plane axial and tangential velocities as well as TKE and ε^* profiles plotted along a horizontal line located 3 mm below the impeller at $y/T=0.14$ are shown in Figs. 12a-d. Larger V_a values are present for the 4PBT than in the V-model impeller in most locations. As can be seen, the profile is broaden in the z -direction for the V-model. Several V_θ peaks are present for both impellers, and the 4PBT model presents larger magnitudes.

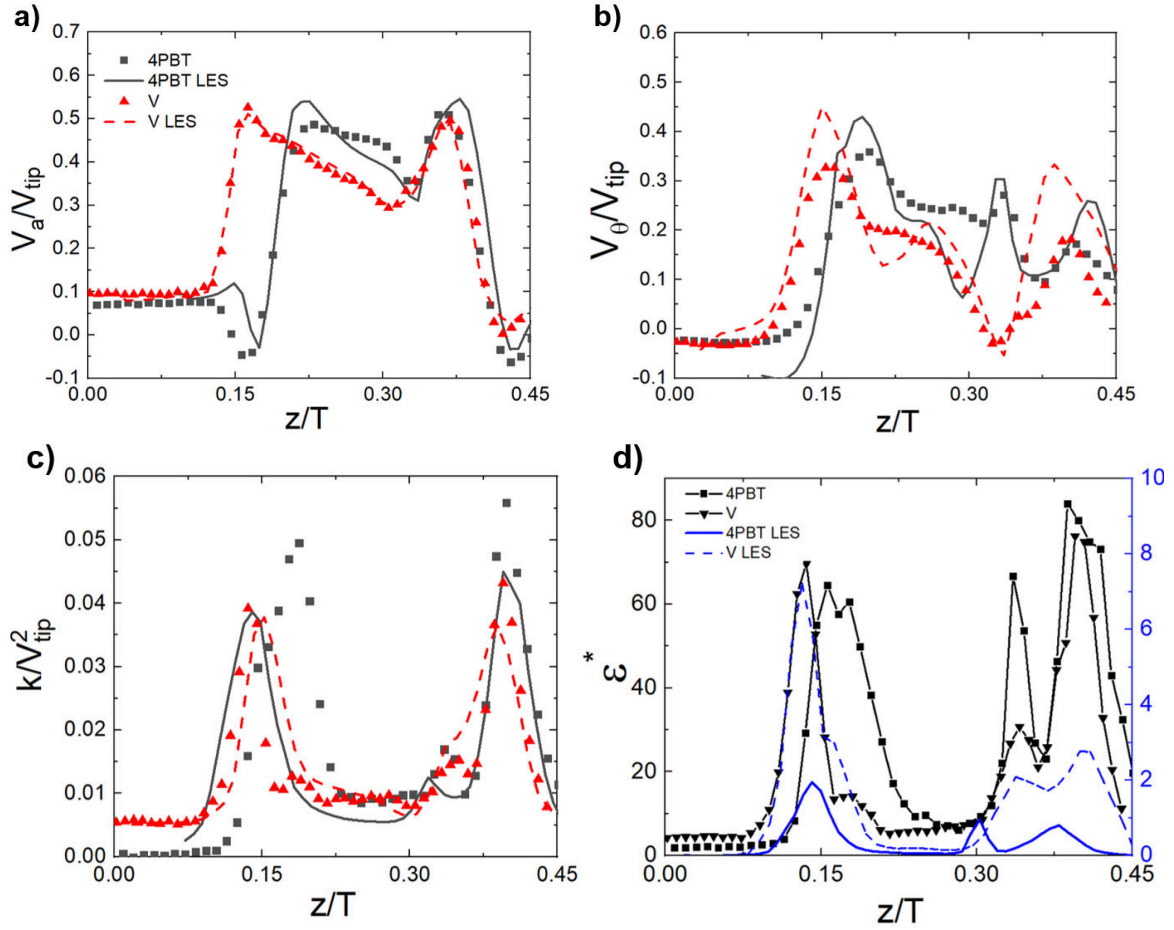


Fig. 12 Mean axial and tangential velocities and turbulent profiles obtained at the mid-blade plane of the impeller blade for both, PIV and LES technique.

Good prediction capabilities were noticed for the LES model, mainly for V_a . However, the peak of high velocity for V_θ , was over-predicted for the V-model in the $0.34 \leq z/T \leq 0.45$ range, and deviations were present in the numerical profile of the 4PBT when compared to

the PIV measurements. Values of TKE for both impellers show two characteristic peaks, which are related to high TKE spots; one at the front and one at the rear impeller region. In most locations, values measured by the regular 4PBT model were larger than those obtained with the V-model. LES-based TKE values of the 4PBT are slightly under-predicted while LES-based values of the V-model exhibit good agreement with the PIV. Finally, the ε^* curve derived from PIV for the 4PBT model shows three peaks, one at the front of the impeller located at $z/T=0.15$ with $\varepsilon^*=63$, and two more at the rear at $z/T=0.35$ and $z/T=0.40$ with $\varepsilon^*=65$ and $\varepsilon^*=80$ respectively. In the front of the impeller region, the V-model shows a similar profile, although slightly shifted. In this case, the peak is located at $z/T=0.14$ with $\varepsilon^*=70$. A second peak is located at the rear of the impeller, matching the location of the rear peak of the 4PBT model, however highly attenuated. This secondary high dissipation spot reaches $\varepsilon^*=25$ while $\varepsilon^*=65$ is obtained for the 4PBT model. The magnitude of ε^* recovers at the third peak, and reaches $\varepsilon^*=73$, at an identical location than for the 4PBT model. Although under-predicted, the LES simulations capture all three high ε^* peaks and their corresponding locations for both impeller. However, the V-model presents larger values than for the 4PBT model.

The profiles of the same flow parameters obtained with PIV and LES, but extracted from the tip plane, are shown in Fig. 13. Now, the V_a values of the V-model show larger magnitudes in comparison to those reached with the 4PBT model in most locations. The peak value of the V-model ($V_a/V_{tip}=0.43$) is about 40% larger than the value attained with the regular 4PBT model. Both impellers exhibit a parabolic behavior, consequence of flow pumping, which is different to that obtained in the mid-plane. As can be seen, LES simulations could capture such phenomenon well. No important differences of V_θ values are present in the tip-plane at

$z/T < 0.24$, although an increase of the V_θ values was observed at $z/T > 0.24$ for the 4PBT model.

One well defined peak and a second and smaller one are present in the TKE profiles, (see Fig. 13c).

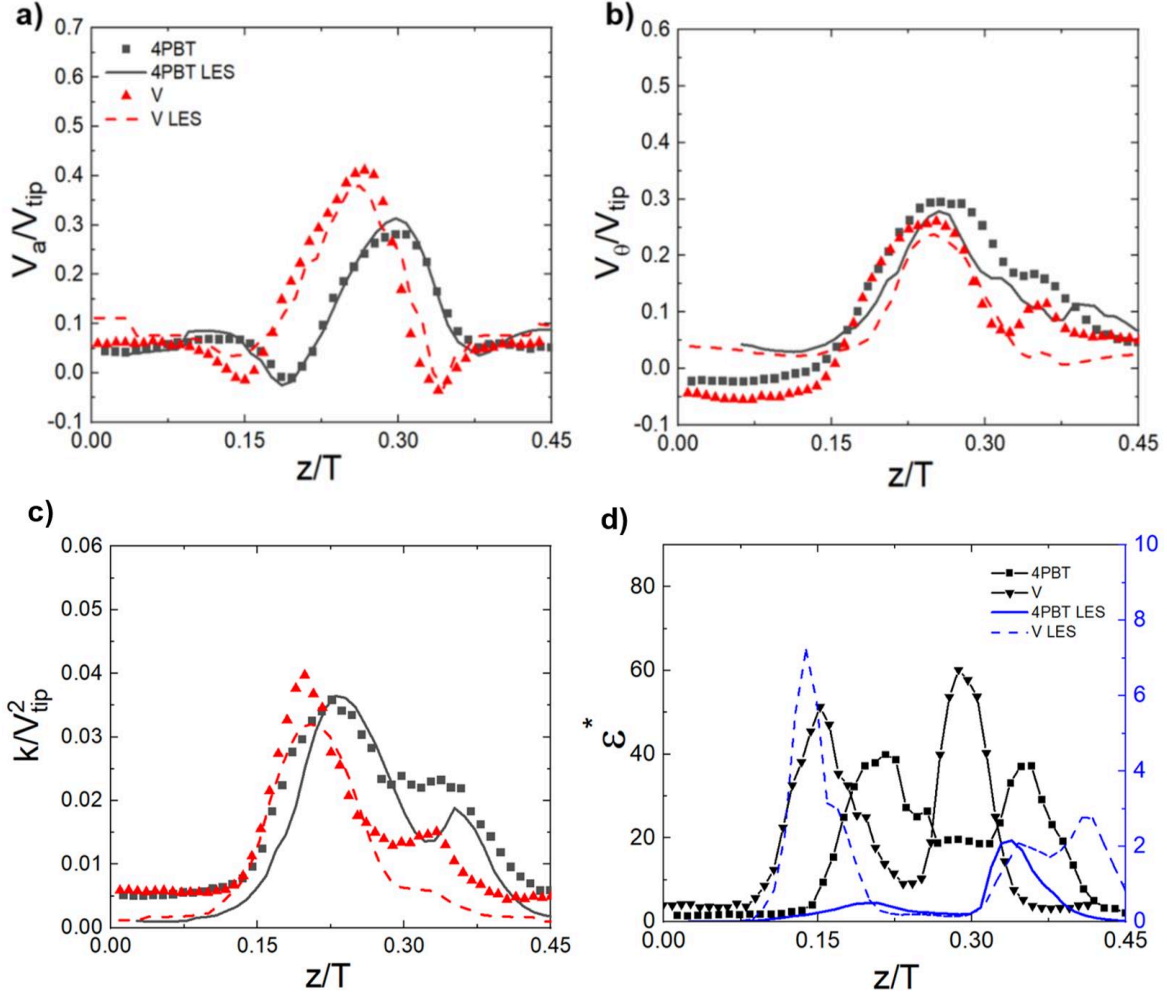


Fig. 13 Mean axial and tangential velocities and turbulent parameters obtained at the tip-blade plane. The profiles were extracted from a line 3 mm below the impeller blade.

For the V-model, the maximum value $k/V_{tip}^2 = 0.041$ is present at $z/T = 0.18$, whereas for the 4PBT model $k/V_{tip}^2 = 0.036$ is obtained at $z/T = 0.23$. The secondary high TKE region of the 4PBT reaches $k/V_{tip}^2 = 0.024$, which is larger than $k/V_{tip}^2 = 0.016$ obtained for the V-model. The LES simulations profiles of the two impeller models followed fairly the first

peaks of TKE, and although sub-predicted, the secondary peaks were also obtained. The experimental ε^* profiles of the 4PBT and the V-model are defined clearly by two high dissipation regions in the front and rear part of the impellers, forming well defined bell shaped regions. The V-model magnitudes were larger than those of the 4PBT model in both zones. For the LES simulations, this dominance in magnitudes of the V-model is also visible. However, the shape of the profiles are different from those obtained numerically, especially for the 4PBT model. In order to extend the assessment, Fig. 14 shows the contour maps obtained by PIV and numerically in the tip plane. It is clear that the intensification of ε^* in the discharge region is caused by the grooved surface.

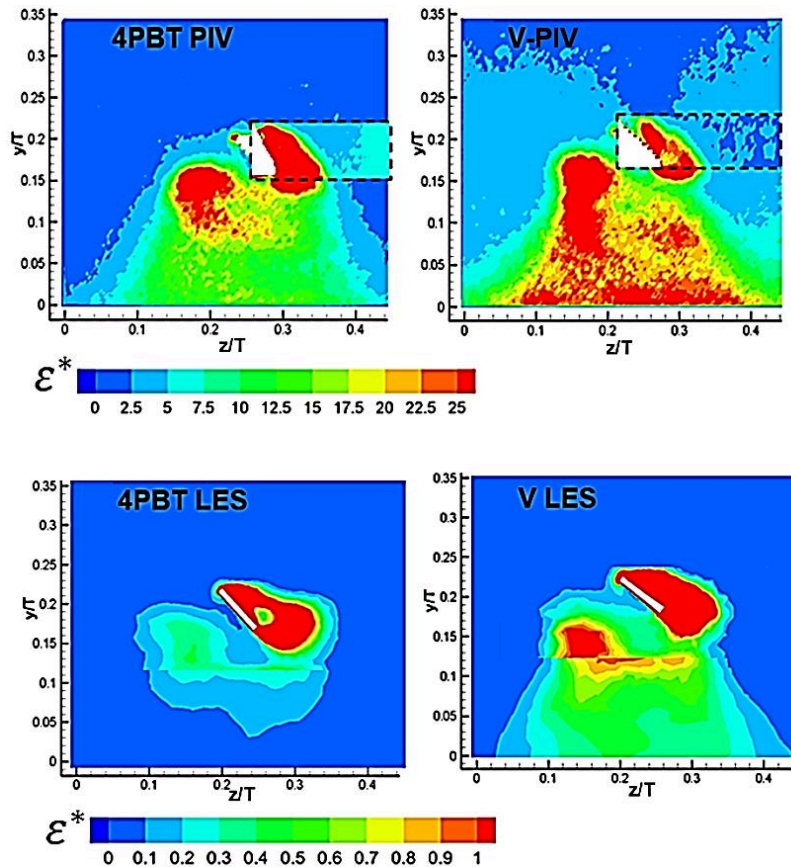


Fig. 14 Turbulence dissipation rate maps derived experimentally and numerically at the tip-blade plane region.

For the 4PBT model, the high ε^* gradient present in front of the blade have lower levels than the rear one. This is reflected in the profile shown in Fig. 13d as one distinct peak around $z/T=0.33$ is visible. Accordingly, V_a , V_θ , ω^* and TKE are fairly predicted by the LES model in all measured planes. Apart from the magnitudes, the trends and gradients of ε^* follow those present in the experimental measurements. The latter supports the idea of G. Lane [4] who suggested that spatially dependent correction factors as function of the mesh resolution could be applied to adjust the dissipation rate in ATRs.

To analyse the performance of the dynamic LES model, a power spectral analysis was applied to the signal of instantaneous radial velocity obtained from 56 impeller passages shown in Fig. 15a. For this purpose, a monitor point located 4 mm below the impeller and near the tip at $r/R=0.95$ was created. According to Fig. 15b, both simulations reproduce the $-5/3$ slope in the inertial subrange calculated as $f/\omega_{rot}=1-20$, which has been related to good predictions of TKE [40].

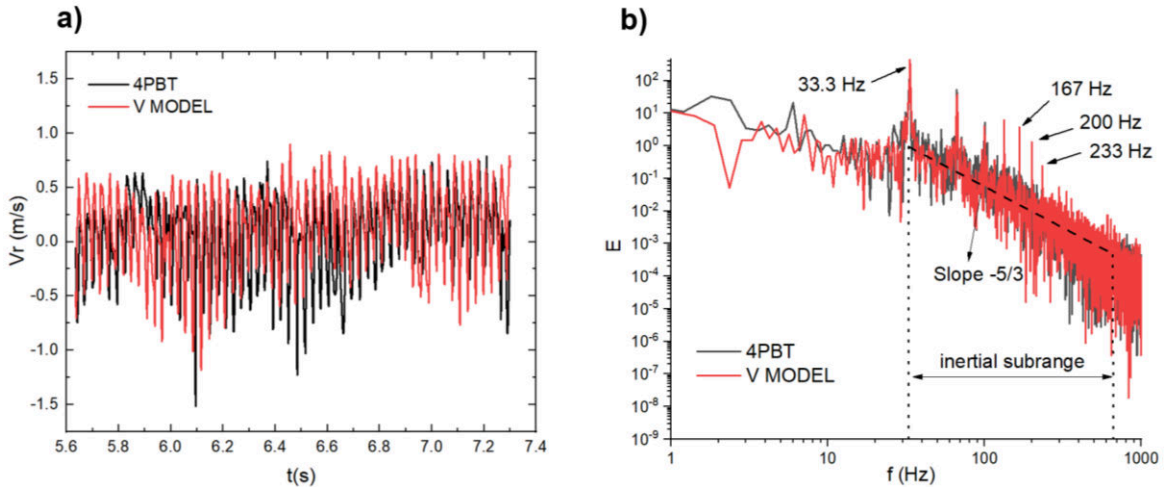


Fig. 15 Turbulence spectrum obtained from a point monitor below the impeller: a) radial velocity from 14 impeller revolutions, b) Kinetic energy spectrum.

Furthermore, the frequency blade passages of 33 Hz, 65 Hz and 95 Hz are visible for both impellers; they are presumably induced by the trailing vortices formed at the tips. However, the V-model clearly indicates the presence of at least three additional frequencies, 167 Hz, 200 Hz and 233 Hz, which are related to secondary vortices near the tip; these are desirable for mixing purposes.

To assess the overall performance of the impellers in the ATR, the N_P and η_E obtained experimentally and through LES, were calculated, see Table 1. The N_P derived from torque-meter measurements indicates that by using the V-model, a reduction of 5 % in power consumption of the drive could be achieved. This was also present in the LES results, although the N_P values were slightly larger than measured experimentally. Similarly, the pumping effectiveness obtained experimentally is slightly better for the V-model. This confirms that the use of grooved walls is beneficial to axial pumping purposes, especially for equipment designed for long time operations. Further geometrical optimization could be even more profitable.

Table 1. Power and pumping effectiveness obtained experimentally and by LES.

Impeller	N_P			η_E	
	Exp.	CFD-torque	CFD- ε	Exp.	CFD
4PBT	1.26	1.31	0.30	0.62	0.56
V-model	1.20	1.24	0.28	0.64	0.59

3.4 Mixing time

Fig. 16 shows the profiles of normalized concentration obtained experimentally and through dynamic LES simulation for the two impellers. The experimental results show that the tracer concentration in the case of the V-model begins to stabilize when the time reaches about 3s,

while in the case of 4PBT, it happens after 4 s. In addition, when the V-model is used, the mixing time is about 11 % lower (see Table 2) than for 4PBT.

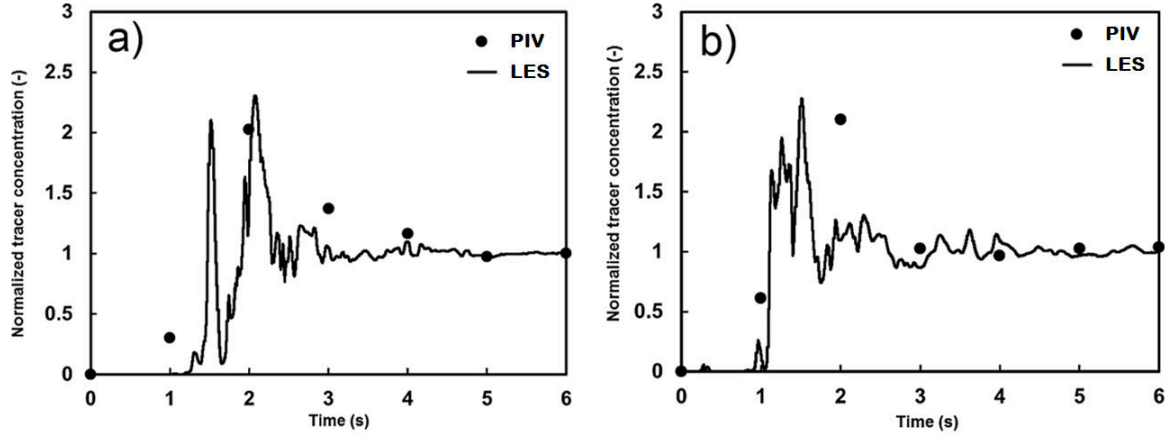


Fig. 16 Profiles of mean normalized concentrations generated by LES simulation and experimental measurements: a) Regular impeller, b) V-grooved model.

This can be due to the larger dissipation energy zones and the increase of the vortical regions induced by the grooves. LES results showed good agreement with experiments from 4s in the 4PBT case, and from 3s for the V-model, i.e. when the flow shows a steady behavior.

To gain an insight into the quick decay of the tracer distribution induced experimentally by the V-grooved model, Fig. 17 shows the blending of the tracer obtained 1 s, 2 s and 3 s after the injection. As can be seen, the tracer is distributed faster for the V-model than for the 4PBT. At 1s, the high concentration zone appears more quickly in the central zone, around the shaft, for the V-model than for the PBT case. At 2s, the enhanced suction effect causes the tracer to reach the V-model impeller faster than in the 4PBT case, showing a faster dispersion (3s). This effect can explain why the mixing time is lower with the V-grooved impeller. The mixing time agreement between the experiment and dynamic LES is thought to be related to the formulation of LES, which resolves directly the larger eddies that contain

most of the flow kinetic energy and are convected by the main recirculation loops formed inside the vessel. In this sense, the overall mixing does not relies only in the dissipative scales related to ε predictions. The sizes of such larger eddies are estimated to range between 1 to 6 mm (proportionally to the grid sizes), being their maximum frequencies estimated of about 100 Hz (related to the adjusted time step for mixing time simulations). According to our results, with such temporal and grid resolutions it was possible to follow the overall experimental tendency.

Table 2. Mixing time predicted by dynamic LES simulation and experimental measurements.

Impeller	Experimental $\theta_{95\%}$ (s)	CFD $\theta_{95\%}$ (s)
V-Grooved	4.0 ± 0.25	4.74
PBT	4.5 ± 0.25	4.77

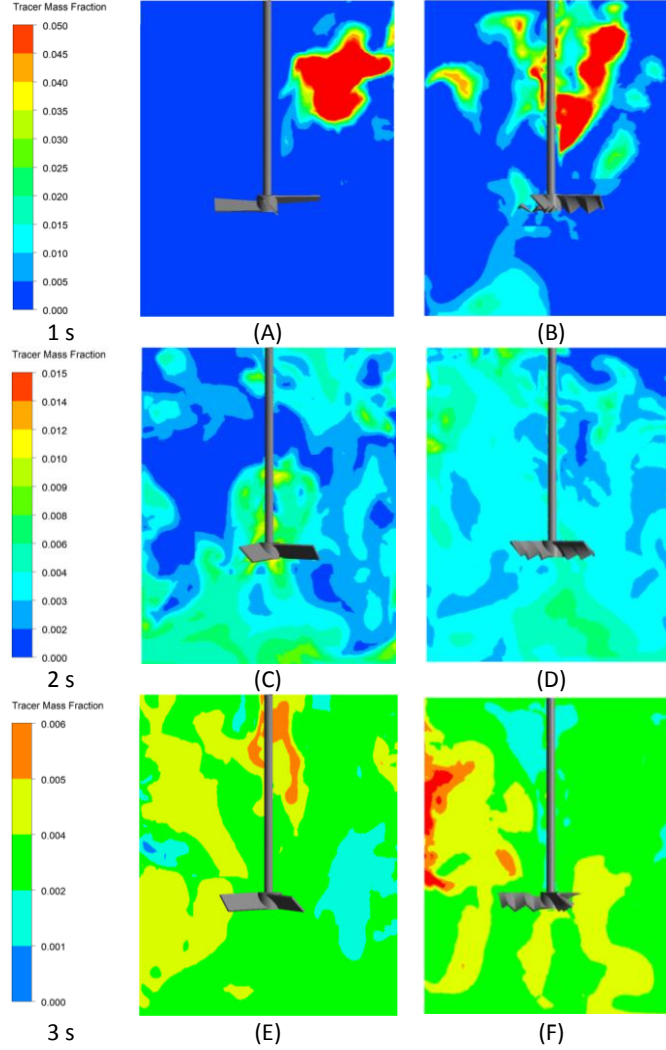


Fig. 17 Contours of the distribution of the tracer at different times after injection. A, C and E is the field of concentration induced by 4PBT. B, D and F are the field induced by V-model.

4. Conclusions

The turbulent flow and mixing characteristics of two axial agitators, one with V-grooves and the other with straight blades, were analyzed i) experimentally by angle resolved PIV with 5° angular intervals and ii), numerically via the dynamic LES model applied to grids of more than three million cells. Velocities and turbulent parameters at the mid and tip blade planes were presented and results compared with LES predictions generated on straight and folded bladed impellers. A dependence of magnitudes for V_a , ω , TKE and ε with the resolved angle

was found for both impeller models, indicating a pulsatile behavior of the mean and turbulent flow.

The levels of ε were higher in the angle resolved range $30^\circ < \theta < 50^\circ$ with the PIV measurements. Although under-predicted magnitudes of ε were predicted by the LES model, the overall gradients were well reproduced; V_a , ω^* and TKE appeared in good agreement with measurements.

In the mid-blade aerodynamic plane, the 4PBT impeller presented higher velocities in comparison to the V-model, whereas in the tip plane, the effect was opposite. It was noticed that vortical interactions were present in the mid-blade plane for both models, with a higher number of zones for the V-model. The latter showed that the flow is tridimensional and complex, and that not only the tip trailing vortices should be investigated when dealing with impeller-based research work. For both planes investigated, all flow parameters, except ε , were adequately reproduced by the LES model.

From the experimental torque measurements, a drag reduction of about 5 % was reported, due to the walls modifications of the V-model (in comparison with a straight blade model), which in turns, showed an increase of pumping effectiveness. Fair N_p values were predicted numerically, but deviations were found when the dissipated numerical power from the volume integral method was applied.

Finally, the mixing time, which is another important parameter to assess the impellers performance, showed a decrease of about 11 % for the V-grooves based impeller. This was a consequence of a better suction that the grooved impeller exerted on the tracer, especially in the first stages of the mixing process.

Further blade optimization could be performed to enhance mixing and improve the results. However, this study has demonstrated that a grooved-blades impeller presents a higher performance than a standard straight blades impeller as it enhances and produces faster mixing.

Acknowledgements

This research did not receive any specific grant from funding agencies in the public, commercial, or not-for-profit sectors. The authors acknowledge the anonymous reviewers assigned to this manuscript for their valuable comments.

References

- [1] J. Aubin, D.F. Fletcher, C. Xuereb, Modeling turbulent flow in stirred tanks with CFD: The influence of the modeling approach, turbulence model and numerical scheme, *Exp. Therm. Fluid Sci.* 28 (2004) 431–445. doi:10.1016/j.expthermflusci.2003.04.001.
- [2] D.A. Deglon, C.J. Meyer, CFD modelling of stirred tanks: Numerical considerations, *Miner. Eng.* 19 (2006) 1059–1068. doi:10.1016/j.mineng.2006.04.001.
- [3] M. Coroneo, G. Montante, A. Paglianti, F. Magelli, CFD prediction of fluid flow and mixing in stirred tanks: Numerical issues about the RANS simulations, *Comput. Chem. Eng.* 35 (2011) 1959–1968. doi:10.1016/j.compchemeng.2010.12.007.
- [4] G.L. Lane, Improving the accuracy of CFD predictions of turbulence in a tank stirred by a hydrofoil impeller, *Chem. Eng. Sci.* 169 (2017) 188–211. doi:10.1016/j.ces.2017.03.061.
- [5] J.B. Joshi, N.K. Nere, C. V. Rane, B.N. Murthy, C.S. Mathpati, A.W. Patwardhan, V. V. Ranade, CFD simulation of stirred tanks: Comparison of turbulence models (Part II: Axial flow impellers, multiple impellers and multiphase dispersions), *Can. J. Chem. Eng.* 89 (2011) 754–816. doi:10.1002/cjce.20465.
- [6] H. Singh, D.F. Fletcher, J.J. Nijdam, An assessment of different turbulence models for predicting flow in a baffled tank stirred with a Rushton turbine, *Chem. Eng. Sci.* 66 (2011) 5976–5988. doi:10.1016/j.ces.2011.08.018.
- [7] X. Jiang, H. Lai, *Numerical Techniques for Direct and Large-Eddy Simulations*, first ed., CRC Press, Florida, 2009. doi:10.1201/9781420075793.
- [8] A. Rasam, G. Brethouwer, P. Schlatter, Q. Li, A. V. Johansson, Effects of modelling,

resolution and anisotropy of subgrid-scales on large eddy simulations of channel flow, *J. Turbul.* 12 (2010) 1–19. doi:10.1080/14685248.2010.541920.

- [9] S.L. Yeoh, G. Papadakis, M. Yianneskis, Numerical simulation of turbulent flow characteristics in a stirred vessel using the LES and RANS approaches with the sliding=deforming mesh methodology, *Trans IChemE.* 82 (2004) 834–848.
- [10] B.N. Murthy, J.B. Joshi, Assessment of standard $k - \epsilon$, RSM and LES turbulence models in a baffled stirred vessel agitated by various impeller designs, *Chem. Eng. Sci.* 63 (2008) 5468–5495. doi:10.1016/j.ces.2008.06.019.
- [11] A. Delafosse, A. Line, J. Morchain, P. Guiraud, LES and URANS simulations of hydrodynamics in mixing tank: Comparison to PIV experiments, *Chem. Eng. Res. Des.* 86 (2008) 1322–1330. doi:10.1016/j.cherd.2008.07.008.
- [12] P. Vlček, B. Kysela, T. Jirout, I. Fořt, Large eddy simulation of a pitched blade impeller mixed vessel - Comparison with LDA measurements, *Chem. Eng. Res. Des.* 108 (2016) 42–48. doi:10.1016/j.cherd.2016.02.020.
- [13] A. Bakker, L.M. Oshinowo, Modelling of Turbulence in Stirred Vessels Using Large Eddy Simulation, *Chem. Eng. Res. Des.* 82 (2004) 1169–1178. doi:10.1205/cerd.82.9.1169.44153.
- [14] R. Zadghaffari, J.S. Moghaddas, J. Revstedt, A mixing study in a double-Rushton stirred tank, *Comput. Chem. Eng.* 33 (2009) 1240–1246. doi:10.1016/j.compchemeng.2009.01.017.
- [15] A. Delafosse, J. Morchain, P. Guiraud, A. Liné, Trailing vortices generated by a Rushton turbine: Assessment of URANS and large Eddy simulations, *Chem. Eng. Res. Des.* 87 (2009) 401–411. doi:10.1016/j.cherd.2008.12.018.
- [16] V. V. Ranade, M. Perrard, L. Sauze, C. N. Xuereb, J. Bertrand, Trailing vortices of Rushton turbine: PIV measurements and CFD simulations with snapshot approach, *Chem. Eng. Res. Des.* 79 (2001) 1–12. doi:10.1205/02638760152721190.
- [17] J.B. Joshi, N.K. Nere, C. V. Rane, B.N. Murthy, C.S. Mathpati, A.W. Patwardhan, V. V. Ranade, CFD simulation of stirred tanks: Comparison of turbulence models. Part I: Radial flow impellers, 89 (2011) 23–82. doi:10.1002/cjce.20446.
- [18] Z. Chara, B. Kysela, J. Konfrst, I. Fort, Study of fluid flow in baffled vessels stirred by a Rushton standard impeller, *Appl. Math. Comput.* 272 (2016) 614–628. doi:10.1016/j.amc.2015.06.044.
- [19] K. V. Sharp, D. Hill, D. Troolin, G. Walters, W. Lai, Volumetric three-component velocimetry measurements of the turbulent flow around a Rushton turbine, *Exp. Fluids.* 48 (2010) 167–183. doi:10.1007/s00348-009-0711-9.
- [20] Y. Bouremel, M. Yianneskis, A. Ducci, On the utilisation of vorticity and strain dynamics for improved analysis of stirred processes, *Chem. Eng. Res. Des.* 87 (2009) 377–385. doi:10.1016/j.cherd.2008.11.016.
- [21] K. Steiros, P.J.K. Bruce, O.R.H. Buxton, J.C. Vassilicos, Power consumption and

- form drag of regular and fractal-shaped turbines in a stirred tank, *AIChE J.* 61 (2014) 1–15. doi:10.1002/aic.
- [22] S. Başbuğ, G. Papadakis, J.C. Vassilicos, Reduced power consumption in stirred vessels by means of fractal impellers, *AIChE J.* 64 (2018) 1485–1499. doi:10.1002/aic.16096.
 - [23] H.C. Lim, S.J. Lee, Flow control of circular cylinders with longitudinal grooved surfaces, *AIAA J.* 40 (2002) 2027–2036. doi:10.2514/2.1535.
 - [24] S.A. Martínez-Delgadillo, A. Alonzo-Garcia, V.X. Mendoza-Escamilla, I. González-Neria, J. Antonio Yáñez-Varela, Analysis of the turbulent flow and trailing vortices induced by new design grooved blade impellers in a baffled tank, *Chem. Eng. J.* 358 (2019) 225–235. doi:10.1016/j.cej.2018.10.015.
 - [25] K. Bittorf, S.M. Kresta, Limits of fully turbulent flow in a stirred tank, in: H.E.A. van den Akker, J.J. Derksen (Eds.), *Proc. 10th Eur. Conf. Mix.* July 2–5, 2000, 1st ed., Delft, The Netherlands, 2000: pp. 17–24. doi:10.1080/00986448108910934.
 - [26] J. Aubin, P. Mavros, D.F. Fletcher, J. Bertrand, C. Xuereb, Effect of axial agitator configuration (up-pumping, down-pumping, reverse rotation) on flow patterns generated in stirred vessels, *Trans IChemE.* 79 (2001) 845–856. doi:10.1205/02638760152721046.
 - [27] A. Gabriele, A.W. Nienow, M.J.H. Simmons, Use of angle resolved PIV to estimate local specific energy dissipation rates for up- and down-pumping pitched blade agitators in a stirred tank, *Chem. Eng. Sci.* 64 (2009) 126–143. doi:10.1016/j.ces.2008.09.018.
 - [28] K. V. Sharp, R.J. Adrian, PIV Study of small-scale flow structure around a Rushton turbine, *AIChE J.* 47 (2001) 766–778. doi:10.1002/aic.690470403.
 - [29] F.R. Khan, C.D. Rielly, D.A.R. Brown, Angle-resolved stereo-PIV measurements close to a down-pumping pitched-blade turbine, *Chem. Eng. Sci.* 61 (2006) 2799–2806. doi:10.1016/j.ces.2005.10.067.
 - [30] J. Sheng, H. Meng, R.O. Fox, A large PIV method for turbulence dissipation rate estimation, *Chem. Eng. Sci.* 55 (2000) 4423–4434.
 - [31] F.R. Khan, Investigation of turbulent flows and instabilities in a stirred vessel using particle image velocimetry, Loughborough University, 2005. <http://ethos.bl.uk/OrderDetails.do?uin=uk.bl.ethos.420146> (accessed August 16, 2017).
 - [32] J. Meyers, P. Sagaut, On the model coefficients for the standard and the variational multi-scale Smagorinsky model, *J. Fluid Mech.* 569 (2006) 287–319. doi:10.1017/S0022112006002850.
 - [33] M. Germano, U. Piomelli, P. Moin, A dynamic subgrid scale eddy viscosity model, *Phys. Fluids A Fluid Dyn.* 3 (1991) 1760–1765.
 - [34] Ansys Fluent V. 12.0, User’s Guide, 2011. doi:10.1111/j.1600-0447.2011.01711.x.

- [35] M. Jahoda, M. Moštěk, A. Kukuková, V. Machoň, CFD Modelling of Liquid Homogenization in Stirred Tanks with One and Two Impellers Using Large Eddy Simulation, *Chem. Eng. Res. Des.* 85 (2007) 616–625. doi:10.1205/cherd06183.
- [36] M. Jian, G. Zhengming, Large Eddy Simulations of Mixing Time in a Stirred Tank, *Chinese J. Chem. Eng.* 14 (2006) 1–7.
- [37] R. Zadghaffari, J.S. Moghaddas, J. Revstedt, Large-eddy simulation of turbulent flow in a stirred tank driven by a Rushton turbine, *Comput. Fluids.* 39 (2010) 1183–1190. doi:10.1016/j.compfluid.2010.03.001.
- [38] V.X. Mendoza-Escamilla, A. Alonzo-García, H.R. Mollinedo, I. González-Neria, J. Antonio Yáñez-Varela, S.A. Martínez-Delgadillo, Assessment of $k-\epsilon$ models using tetrahedral grids to describe the turbulent flow field of a PBT impeller and validation through the PIV technique, *Chinese J. Chem. Eng.* (2018). doi:10.1016/j.cjche.2018.02.012.
- [39] Z. Li, Y. Bao, Z. Gao, PIV experiments and large eddy simulations of single-loop flow fields in Rushton turbine stirred tanks, *Chem. Eng. Sci.* 66 (2011) 1219–1231. doi:10.1016/j.ces.2010.12.024.
- [40] J. Gimbut, C.D. Rielly, Z.K. Nagy, J.J. Derksen, Detached eddy simulation on the turbulent flow in a stirred tank, *AIChE J.* 00 (2011) 1–18. doi:10.1002/aic.
- [41] S. Baldi, A. Ducci, M. Yianneskis, Determination of dissipation rate in stirred vessels through direct measurement of fluctuating velocity gradients, *Chem. Eng. Technol.* 27 (2004) 275–281. doi:10.1002/ceat.200401979.
- [42] P. Saarenrinne, M. Piirto, H. Eloranta, Experiences of turbulence measurement with PIV*, *Meas. Sci. Technol.* 12 (2001) 1904–1910. doi:10.1088/0957-0233/12/11/320.